ADVANCES IN ATMOSPHERIC SCIENCES, VOL. 41, FEBRUARY 2024, 193–208

• **Original Paper** •

Assessing the Performance of CMIP6 Models in Simulating Droughts across Global Drylands※

Xiaojing YU[1,4], Lixia ZHANG*[1,2], Tianjun ZHOU[1,3], and Jianghua ZHENG[4]

[1]*LASG, Institute of Atmospheric Physics, Chinese Academy of Sciences, Beijing* 100029, *China*

[2]*Collaborative Innovation Center on Forecast and Evaluation of Meteorological Disasters, Nanjing University of Information Science & Technology, Nanjing* 210044, *China*

[3]*University of Chinese Academy of Sciences, Beijing* 100049, *China*

[4]*College of Geography & Remote Sensing Sciences, Xinjiang University, Urumqi* 830046, *China*

(Received 28 September 2022; revised 12 January 2023; accepted 28 January 2023)

ABSTRACT

Both the attribution of historical change and future projections of droughts rely heavily on climate modeling. However, reasonable drought simulations have remained a challenge, and the related performances of the current state-of-the-art Coupled Model Intercomparison Project phase 6 (CMIP6) models remain unknown. Here, both the strengths and weaknesses of CMIP6 models in simulating droughts and corresponding hydrothermal conditions in drylands are assessed. While the general patterns of simulated meteorological elements in drylands resemble the observations, the annual precipitation is overestimated by ~33% (with a model spread of 2.3%–77.2%), along with an underestimation of potential evapotranspiration (PET) by ~32% (17.5%–47.2%). The water deficit condition, measured by the difference between precipitation and PET, is 50% (29.1%–71.7%) weaker than observations. The CMIP6 models show weaknesses in capturing the climate mean drought characteristics in drylands, particularly with the occurrence and duration largely underestimated in the hyperarid Afro-Asian areas. Nonetheless, the drought-associated meteorological anomalies, including reduced precipitation, warmer temperatures, higher evaporative demand, and increased water deficit conditions, are reasonably reproduced. The simulated magnitude of precipitation (water deficit) associated with dryland droughts is overestimated by 28% (24%) compared to observations. The observed increasing trends in drought fractional area, occurrence, and corresponding meteorological anomalies during 1980–2014 are reasonably reproduced. Still, the increase in drought characteristics, associated precipitation and water deficit are obviously underestimated after the late 1990s, especially for mild and moderate droughts, indicative of a weaker response of dryland drought changes to global warming in CMIP6 models. Our results suggest that it is imperative to employ bias correction approaches in drought-related studies over drylands by using CMIP6 outputs.

Key words: droughts, hydrothermal conditions, drylands, CMIP6, model evaluation

Citation: Yu, X. J., L. X. Zhang, T.-J. Zhou, and J. H. Zheng, 2024: Assessing the performance of CMIP6 models in simulating droughts across global drylands. *Adv. Atmos. Sci.*, **41**(2), 193–208, https://doi.org/10.1007/s00376-023-2278-4.

Article Highlights:

- The water deficit condition over drylands in CMIP6 models is weaker than observations due to overestimated climate mean precipitation and underestimated PET.
- CMIP6 models overestimate drought intensity but underestimate drought occurrence and duration in drylands, which may result from more severe water deficits during droughts.
- The observed increasing trends of dryland droughts and contributions of precipitation and PET are well simulated by CMIP6, albeit with a weaker response to global warming after the 1990s than observations.

1. Introduction

Drought is a slow-onset but damaging hydroclimatic hazard with broad spatiotemporal scales (Gill and Malamud, 2014; Ault, 2020). Severe droughts can bring cascading impacts not only on ecosystems (Piao et al., 2019) and environmental systems (Vicente-Serrano et al., 2020) but also

※ This paper is a contribution to the special issue on Causes, Impacts, and Predictability of Droughts for the Past, Present, and Future.

* Corresponding author: Lixia ZHANG
Email: lixiazhang@mail.iap.ac.cn

on socioeconomic development (WMO, 2021). Drought-prone drylands, characterized by scarce precipitation and high atmospheric evaporative demand [measured by potential evapotranspiration (PET)], occupy ~41% of global terrestrial land and sustain ~38% of the global population (White and Nackoney, 2003). Due to the vulnerable ecosystems and low societal resilience, drylands are susceptible to greater threats than humid regions once hit by severe droughts, such as land degradation and desertification, water and food deficits, population migrations, and international disputes (Sivakumar et al., 2013; Davies et al., 2016; Cherlet et al., 2018; WMO, 2021). Therefore, understanding how droughts are changing is critical to policy-making for climate adaptation and mitigation activities in dryland countries.

Global climate models (GCMs) are useful tools for investigating the climate response to different forcings and for climate prediction and projection. The Coupled Model Intercomparison Project (CMIP) has provided a fundamental basis for the study of drought. Comprehensive assessments of the strengths and weaknesses of GCMs are of great importance for understanding how drought has changed in the past, the characteristics of present drought, and what is expected in the future (Eyring et al., 2019). Issues related to drought and aridity essentially depend on whether water balance is in surplus or deficit, which is determined by the balance between precipitation and PET (Sherwood and Fu, 2014; Ault, 2020). Thus, a reasonable simulation for the meteorological factors that drive droughts is the premise for reliable future projections of drought and aridity. So far, great efforts have been made to evaluate the performances of CMIP models in reproducing meteorological factors and basic drought characteristics. It has been demonstrated that most CMIP models can capture the dominant features of the spatiotemporal changes in temperature (Zhao et al., 2014) and PET (Liu et al., 2020) but underestimate their increasing trends. Yet, the GCMs have limited capabilities in simulating the evolution of precipitation, underestimating its variability and long-term trends (Zhao et al., 2014).

The ability of GCMs to simulate drought and aridity is usually evaluated by using multiple indices derived from different hydroclimatic elements (Dai, 2011; Peters-Lidard et al., 2021). Based on the self-calibrated Palmer Drought Severity Index (scPDSI), the CMIP Phase 3 (CMIP3) and Phase 5 (CMIP5) models well reproduce the observed long-term changes in global and hemispheric drought areas but show discrepancies in the regional trend patterns (Zhao and Dai, 2017). Employing a standardized drought index approach, Ukkola et al. (2018) addressed the agreement of CMIP5 model variations with drought metrics (i.e., severity and duration) in simulating different types of droughts (i.e., precipitation, runoff, and soil moisture). The simulation biases further lead to large uncertainties in global drought projections, especially over arid regions, even in the latest CMIP Phase 6 (CMIP6) models (Cook et al., 2020; Ukkola et al., 2020; Zhao and Dai, 2022). Until now, less effort has been devoted to evaluating CMIP6 models in simulating drought-related hydrothermal conditions in global drylands.

The primary motivation of this study is to evaluate the performances of the new CMIP6 models in the simulation of droughts and the associated hydro-meteorological conditions over global drylands. We intend to address the following questions: 1) How do CMIP6 models perform in simulating droughts and primary meteorological elements in drylands? 2) Are CMIP6 models able to capture the responses of dryland droughts and associated meteorological elements to global warming?

The remainder of this paper is organized as follows. Section 2 describes data and methods used in this study. Subsequently, elaborate evaluation results are illustrated in section 3. To the end, we summarize and discuss results in section 4.

2. Data and methods

2.1. *Observation and CMIP6 simulation datasets*

We used the monthly observations from Climatic Research Unit gridded Time Series Version 4.03 (CRU TS v.4.03) with a horizontal resolution of 0.5° latitude × 0.5° longitude as validation datasets (Harris et al., 2020). The three variables of monthly precipitation, temperature, and PET from 1960–2018, were employed in this study.

Monthly PET values in CMIP6 simulations were calculated following the Penman-Monteith approach (Penman, 1948; Monteith, 1965), which is derived based on surface moisture and energy balance and recommended by the Food and Agricultural Organization (FAO) of the United Nations (Allen et al., 1998). The detailed calculation of PET is as follows:

$$\mathrm{PET} = \frac{0.408\Delta(R_n - G) + \gamma \dfrac{900}{T_{as} + 273} u_2 (e_s - e_a)}{\Delta + \gamma(1 + 0.34u_2)}, \quad (1)$$

where PET (mm d^{-1}) is the reference evapotranspiration rate, R_n (MJ m^{-2} h^{-1}) and G (MJ m^{-2} h^{-1}) are the net radiation and soil heat flux, respectively. T_{as} (°C) is 2 m air temperature, u_2 (m s^{-1}) is 2 m wind speed, Δ (kPa $°C^{-1}$) represents the slope of the saturation vapor pressure–temperature relationship, and γ (kPa $°C^{-1}$) is the psychrometric constant.

Specifically, e_s–e_a (kPa) represents the difference between saturation vapor pressure (e_s) and actual vapor pressure (e_a), i.e., vapor pressure deficit (VPD). In CMIP6 simulations, e_s and e_a can be calculated following Eqs. (2–3):

$$e_s = 0.6108 \exp\left(\frac{17.27 T_{as}}{(T_{as} + 237.3)}\right), \quad (2)$$

$$e_a = e_s \times \frac{\mathrm{RH}}{100}, \quad (3)$$

where RH (%) is relative humidity.

According to Eqs. (1–3), the relevant input variables

for calculating PET from CMIP6 outputs include the near-surface air temperature (tas), relative humidity (hurs), 10 m wind speed (uas, vas), longwave (rlds, rlus), and shortwave (rsds, rsus) radiation. Thus, we selected the historical simulations for the period 1980–2014 from 27 CMIP6 models (Eyring et al., 2016; Table 1) to assess their respective performance. This is the maximum number of models with available data that allow us to diagnose the PET simulation. Only the first realization of each model was employed in this study. To facilitate calculations and comparisons, all outputs were first re-gridded to 1.5° latitude × 1.5° longitude via a bilinear interpolation.

2.2. *Definition of drylands and droughts*

Drylands are generally measured by the aridity index (AI; Middleton and Thomas, 1992; Hulme, 1996), which is defined as the ratio of annual precipitation to PET (i.e., AI = *P*/PET). In this study, we identified global drylands in both observations and simulations as regions with an annually averaged AI, based on 1960–2018 observations, of less than 0.65 following previous studies (Feng and Fu, 2013; Huang et al., 2016).

The drought index is measured by the Standardized Precipitation Evapotranspiration Index (SPEI), which is defined as a log-logistic probability distribution of the difference between precipitation and PET (*P*–PET) (Vicente-Serrano et al., 2010). The observed and simulated SPEI were calculated using monthly precipitation and PET from CRU and CMIP6 outputs, respectively. The SPEI can be calculated at different time scales (⩾1 month). For the responses of arid biomes to droughts on short timescales (Vicente-Serrano et al., 2013), we employed the 6-month SPEI (SPEI-06) to identify drought events in this study. Droughts were then divided into four categories, i.e., above mild (SPEI⩽–0.5), above moderate (SPEI⩽–1.0), above severe (SPEI⩽–1.5), and above extreme (SPEI⩽–2.0) droughts, which correspond to mild, moderate, severe and extreme drought, respectively, in this study.

Four drought metrics, including the intensity, occurrence, duration, and fraction of affected area, for each drought category, were calculated to assess drought characteristics. Drought intensity is the mean SPEI of a drought event, occurrence (month yr^{-1}) is the number of months under drought condition in a year, duration (months) is the months for an individual drought event, and fraction of affected area (%) is the percentage of area under drought con-

Table 1. Introduction to the 27 CMIP6 models used in this study.

No.	Model Name	Institute, Country	Resolution (Lat×Lon×Level)
1	ACCESS-CM2	Commonweaalth Scientific and Industrial Research Organization (CSIRO) and Bureau of Meteorology (BoM), Australia	144×192×85
2	ACCESS-ESM1-5		145×192×38
3	BCC-CSM2-MR	Beijing Climate Center (BCC), China	160×320×46
4	CanESM5	Canadian Centre for Climate Modelling and Analysis (CCCma), Canada	64×128×49
5	CMCC-CM2-SR5	The Euro-Mediterranean Centre on Climate Change (CMCC)	192×288×47
6	CNRM-CM6-1	Centre National de Recherches Meteorologiques/Centre Europeen de Recherche et Formation Avancees en Calcul Scientifique (CNRM-CERFACS), France	128×256×91
7	EC-Earth3	EC-Earth-Consortium, Europe	256×512×91
8	EC-Earth3-CC	EC-Earth-Consortium, Europe	256×512×91
9	EC-Earth3-Veg	EC-Earth-Consortium, Europe	256×512×91
10	EC-Earth3-Veg-LR	EC-Earth-Consortium, Europe	160×320×62
11	FGOALS-f3-L	Institute of Atmospheric Physics, Chinese Academy of Sciences (IAP-CAS), China	180×288×32
12	GFDL-CM4	NOAA's Geophysical Fluid Dynamics Laboratory (NOAA-GFDL), USA	180×288×33
13	GFDL-ESM4	NOAA's Geophysical Fluid Dynamics Laboratory (NOAA-GFDL), USA	180×288×49
14	GISS-E2-1-G	NASA Goddard Institute for Space Studies (NASA-GISS), USA	90×144×40
15	HadGEM3-GC31-LL	Met Office Hadley Centre (MOHC), UK	144×192×85
16	HadGEM3-GC31-MM	Met Office Hadley Centre (MOHC), UK	324×432×85
17	INM-CM4-8	Institute for Numerical Mathematics (INM), Russia	120×180×21
18	INM-CM5-0	Institute for Numerical Mathematics (INM), Russia	120×180×73
19	IPSL-CM6A-LR	Institute Pierre Simon Laplace (IPSL), France	143×144×79
20	KACE-1-0-G	National Institute of Meteorological Sciences, Korea Meteorological Administration (NIMS-KMA), Korea	144×192×63
21	KIOST-ESM	Korea Institute of Ocean Science and Technology (KIOST), Korea	96×192×32
22	MIROC6	Atmosphere and Ocean Research Institute (AORI, the University of Tokyo), National Institute for Environmental Studies, and Japan Agency for Marine-Earth Science and Technology (JAMSTEC), Japan	128×256×80
23	MIROC-ES2L		64×128×62
24	MPI-ESM1-2-HR	Max Planck Institute for Meteorology (MPI-M), Germany	192×384×95
25	MPI-ESM1-2-LR	Max Planck Institute for Meteorology (MPI-M), Germany	96×192×47
26	MRI-ESM2-0	Meteorological Research Institute (MRI), Japan	160×320×80
27	UKESM1-0-LL	Met Office Hadley Centre (MOHC), UK	144×192×85

dition relative to the global dryland area (Ukkola et al., 2018).

To represent drought-related hydrothermal conditions, four meteorological variables, including precipitation, temperature, PET, and *P*–PET, were examined. To exclude the seasonal cycle, the anomaly for each variable was first obtained as follows:

$$\mathrm{Anom}_{i,j} = x_{i,j} - \overline{x}_j \,, \tag{4}$$

where i is the year ranging from 1980 to 2014, j is the month ranging from January to December, $x_{i,j}$ is the meteorological variable of month j for year i, and $\overline{x}_j$ is the 1980–2014 climatology for month j.

Considering SPEI-06 represents the water balance for the preceding 6 months, we further calculated the previous 6-month average of the anomaly for each meteorological variable. Each meteorological anomaly during the four drought categories was then extracted and analyzed.

2.3. *Model evaluation metrics*

Droughts and the corresponding primary meteorological elements were assessed in terms of their climatology, interannual variability, and long-term trends for the period 1980–2014. The interannual variability is measured by the temporal standard deviation (SD). The long-term trend is estimated by Theil-Sen non-parametric statistics (Sen, 1968; Theil, 1992) and is tested if the monotonic trend is robust by the Mann-Kendall non-parametric method (Mann, 1945; Kendall, 1955).

To quantify the performances of the 27 CMIP6 models, we calculated the pattern correlation coefficients (PCC) and root-mean-square error (RMSE) between the simulation and observation, representing the spatial distribution similarity and model biases, respectively. Following Seo et al. (2013), we employed a skill score to evaluate both the PCC and normalized spatial SD, calculated as follows:

$$S = \frac{4(1+\mathrm{PCC})}{\left(\sigma + \frac{1}{\sigma}\right)^2 (1+\mathrm{PCC}_0)} \,, \tag{5}$$

where PCC is the pattern correlation coefficient between simulation and observation, σ is the simulated spatial SD divided by the observed SD (i.e., normalized spatial SD), and PCC_0 is the maximum achievable correlation (set to 1 here).

3. Results

3.1. *Simulation on primary meteorological elements in drylands*

In this section, we first evaluate the performances of CMIP6 models in reproducing the meteorological elements across global drylands, given the aforementioned meteorological anomalies as the main drought drivers. Figure 1 shows the spatial patterns of the climatology of the annual precipitation, temperature, PET, and *P*–PET in drylands from the observations, the simulated CMIP6 multi-model ensemble mean (MME), and their respective differences. Observations show the climate mean annual precipitation, temperature, and PET averaged over global dryland regions to be 328 mm, 17.8°C, and 1580 mm, respectively (Figs. 1a, d, g). Because the atmospheric evaporative demand is higher than the water supply, global drylands are completely under water deficit conditions, with *P*–PET reaching –1252 mm on average (Fig. 1j). The climatological values of the four meteorological elements are unevenly distributed across global drylands. The annual precipitation amount agrees with the spatial pattern of aridity, with the least rainfall (<25 mm) observed in the hyperarid North Africa-Middle East and western Australia areas, while relatively greater rainfall (>500 mm) occurred in the semihumid and semiarid Sahel, India Peninsula, and northern Australian areas (Fig. 1a). The climate mean annual temperature, PET, and *P*–PET show similar patterns to each other, particularly with the highest temperature (>28°C), atmospheric evaporative demand (>2400 mm) and the most severe water deficit condition (<–2400 mm) in the hyperarid North Africa-Middle East and western Australian regions (Figs. 1d, g, j).

The spatial distributions for the climate mean states of the four meteorological elements from CMIP6 MME agree well with the observations, with the PCC of simulated annual precipitation, temperature, PET, and *P*–PET reaching 0.8, 1.0, 0.8, and 0.8, respectively (Figs. 1b, e, h, k). The annual precipitation is overestimated in most drylands except the northern African, Middle East, and India peninsula regions, on average by 107.6 mm (~33% of observed climate mean), with the RMSE reaching 250.5 mm (Figs. 1b, c). In contrast, the annual temperature and PET in drylands are systematically underestimated by CMIP6 models (Figs. 1e, f, h, i), especially for PET with an area average that is 500 mm (~32%) lower than observations (Figs. 1h, i). Due to the combination of overestimated precipitation and underestimated PET, CMIP6 MME shows a systematic overestimation of *P*–PET across all dryland areas, as evidenced by an area mean (–607 mm) that is about 48% less than the observation (–1252 mm) (Figs. 1k, l). The largest bias also occurs in the hyperarid North Africa-Middle East and western Australia regions, exceeding 1500 mm, thereby indicating much weaker water deficit conditions in drylands simulated by CMIP6 models relative to observations. According to Eq. (1), PET is determined by T_{as}, e_{a}, R_{n}, and u_2. Considering the observational data availability to calculate PET in CRU TS v.4.03, we checked the relative contributions of the four factors to PET bias and found that the systematic underestimation in PET mainly comes from biases in radiation and wind speed, especially over the hyperarid North Africa and Middle East drylands (figures not shown).

We further examine the performances of CMIP6 models in the simulation of interannual variability of the four meteorological elements depicted in Fig. 2. The observed are-aver-

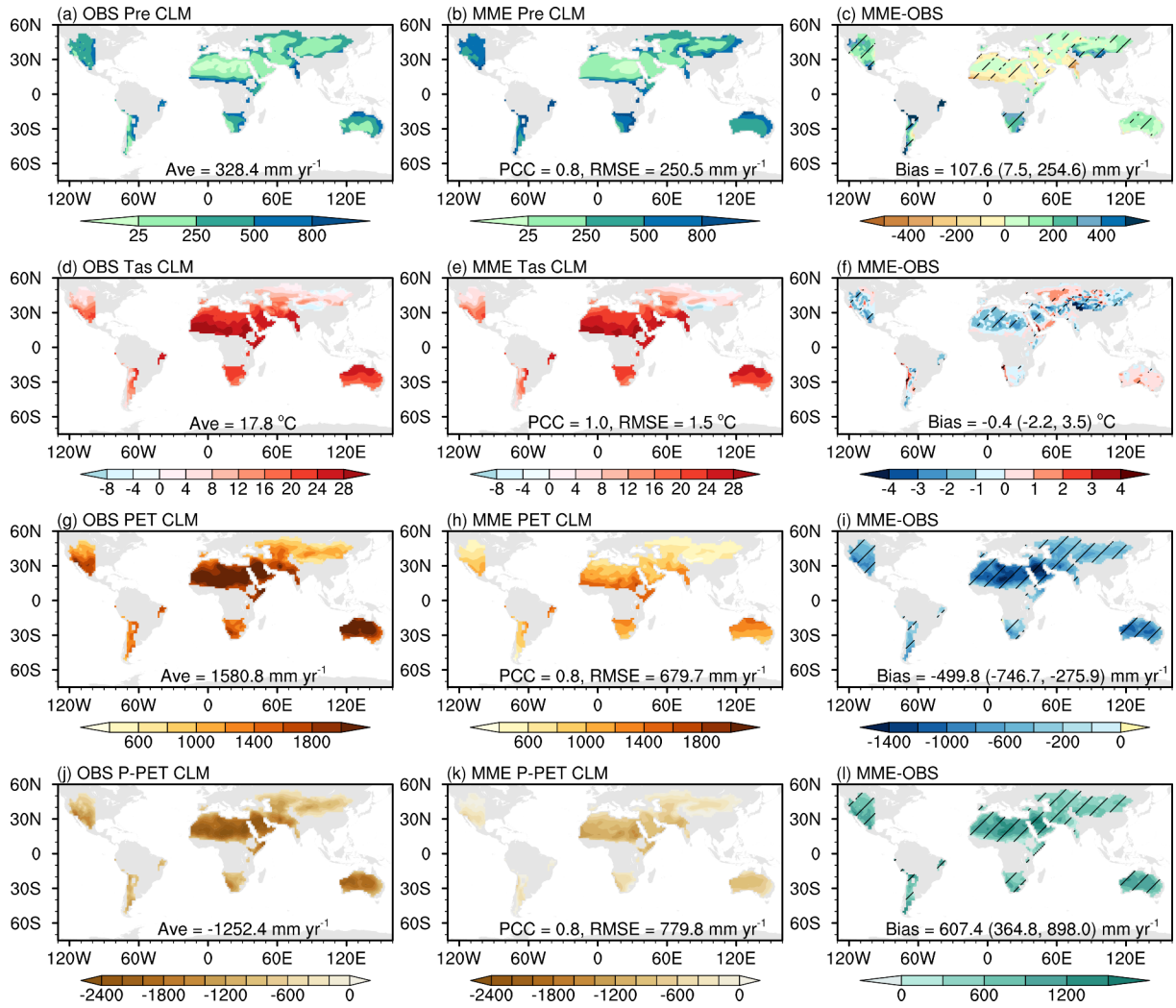

Fig. 1. Spatial patterns of observed and simulated climatology in four meteorological elements across global drylands during 1980–2014. (a–c) Annual precipitation (units: mm yr^{-1}), (d–f) annual mean temperature (units: °C), (g–i) annual potential evapotranspiration (PET, units: mm yr^{-1}), (j–l) annual water balance (*P*–PET, units: mm yr^{-1}). The three columns depict observation, CMIP6 multi-model ensemble mean (MME), and biases. Slant hatchings in the right column denote that 21/27 models are of the same sign, and area-averaged biases are presented as MME and inter-model range between minimum and maximum, respectively.

aged, interannual variability of annual precipitation, temperature, PET, and *P*–PET in drylands is 69.2 mm yr^{-1}, 0.5 °C yr^{-1}, 39.9 mm yr^{-1} and 95.9 mm yr^{-1}, respectively, with obvious regional differences (Figs. 2a, d, g, j). The interannual variability in both precipitation (Fig. 2a) and *P*–PET (Fig. 2j) shows a high consistency with the annual precipitation climatology (Fig. 1a), with the lowest SD (<20 mm yr^{-1}) observed in the hyperarid regions and the largest SD (>200 mm yr^{-1}) in the semiarid and semihumid areas. As for annual mean temperature (Fig. 2d), the observed interannual variability in the northern mid-latitude drylands (>1.0°C yr^{-1}) is notably higher than the tropical and Southern Hemisphere drylands (0.2°C yr^{-1}–0.4°C yr^{-1}). The observed interannual variability of PET (Fig. 2g) is generally below 60 mm yr^{-1} over most drylands, except for the North American (>100 mm yr^{-1}), central Asian, and western Australian areas (~70 mm yr^{-1}).

CMIP6 models well reproduce the spatial patterns for the interannual variability of precipitation, temperature, and *P*–PET, but fail to capture that for PET, with their PCC of simulation reaching 0.9, 0.8, 0.8, and only 0.1, respectively (Figs. 2b, e, h, k). Overall, CMIP6 models overestimate the interannual variability of precipitation, temperature, and *P*–PET in most drylands, on average by 25.6 mm yr^{-1} (~37% of observed SD) and 0.2°C yr^{-1} (~38%), and 18.7 mm yr^{-1} (~19%), respectively, while underestimate that of PET by –6.9 mm yr^{-1} (~17%). For precipitation (Fig. 2c) and temperature (Fig. 2f), the overestimations of their interannual variability are widespread across most drylands. The largest biases are seen in the Southern Hemisphere for precipitation (>60 mm yr^{-1}) and in many dryland regions for temperature (>0.4°C yr^{-1}). Biases for the interannual variability in PET (Fig. 2i) and *P*–PET (Fig. 2l) present heterogeneous patterns. For PET, the largest overestimation (>40 mm yr^{-1}) is

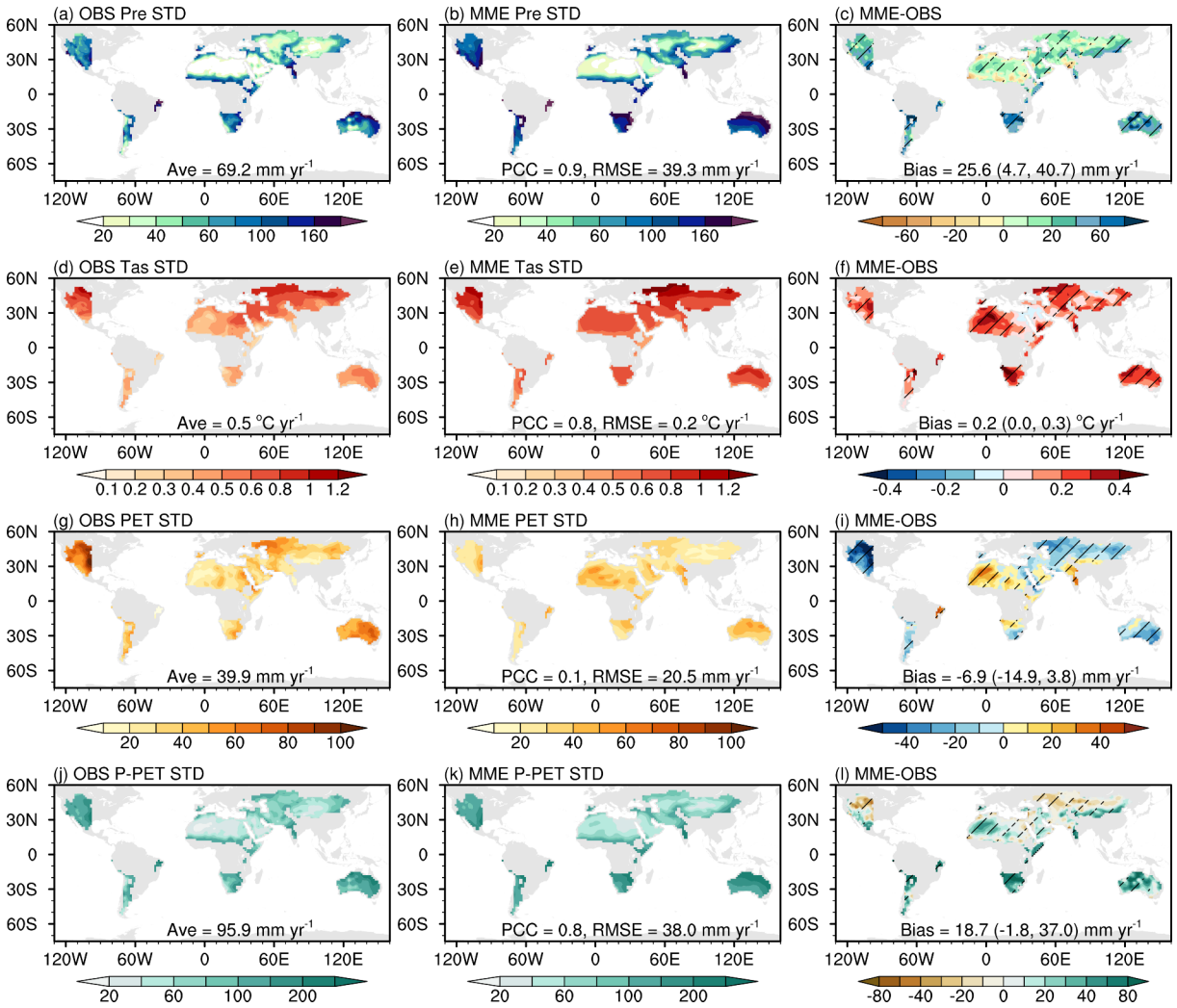

Fig. 2. Same as in Fig. 1, but for the interannual variability of four meteorological elements during 1980–2014. (a–c) Annual precipitation (units: mm yr^{-1}), (d–f) annual mean temperature (units: °C yr^{-1}), (g–i) annual potential evapotranspiration (PET, units: mm yr^{-1}), (j–l) annual water balance (*P*–PET, units: mm yr^{-1}).

seen in the western North Africa and India Peninsula regions, while the largest underestimation (<–50 mm yr^{-1}) is located over the North American drylands. For *P*–PET, positive biases within 20–80 mm yr^{-1} are widely seen over most drylands except for slight negative biases (~20 mm yr^{-1}) in the northern mid-latitudes. Notably, the CMIP6 models well simulate the spatial patterns of the interannual variability in precipitation and *P*–PET but perform poorly for PET, suggesting that the interannual variability of *P*–PET is dominated by precipitation.

We extend our analysis to the long-term trends over the time period 1980–2014 in Fig. 3. The observation presents an overall increasing trend in the annual precipitation, temperature, and PET across global drylands, with average rates of 11.3 mm $(35\ yr)^{-1}$, 0.85°C $(35\ yr)^{-1}$ and 48.6 mm $(35\ yr)^{-1}$, respectively (Figs. 3a, d, g). The trend in annual precipitation shows heterogeneous patterns, with a trend of wetting [>100 mm $(35\ yr)^{-1}$] in the Sahel, South African, India Peninsula, and northern Australian drylands with drying [<–70 mm $(35\ yr)^{-1}$] in many other dryland areas. The warming rate is particularly faster in the Afro-Asian drylands [>1.5°C $(35\ yr)^{-1}$] compared to the other drylands. Because the rising atmospheric evaporative demand is partly offset by increased precipitation, the annual *P*–PET has generally declined at –36 mm $(35\ yr)^{-1}$ over global drylands (Fig. 3j), showing a similar pattern with annual precipitation. The decreasing trend in the annual *P*–PET suggests deteriorating water deficit conditions over most drylands except for those regions with significant wetting trends.

Although CMIP6 simulations agree with the observation on the sign of the long-term trend in the four meteorological elements over global drylands, the regional patterns are poorly reproduced, as evidenced by the low PCC of simulations within 0.2–0.5 and large RMSEs (Figs. 3b, e, h, k). The biases for the long-term trend in all meteorological elements show obvious regional dependence. The simulated annual precipitation presents an increasing trend over the observed drying regions, including most Northern Hemispheric and South American drylands; thus, the long-term trend is overestimated by about 80 mm $(35\ yr)^{-1}$, at most

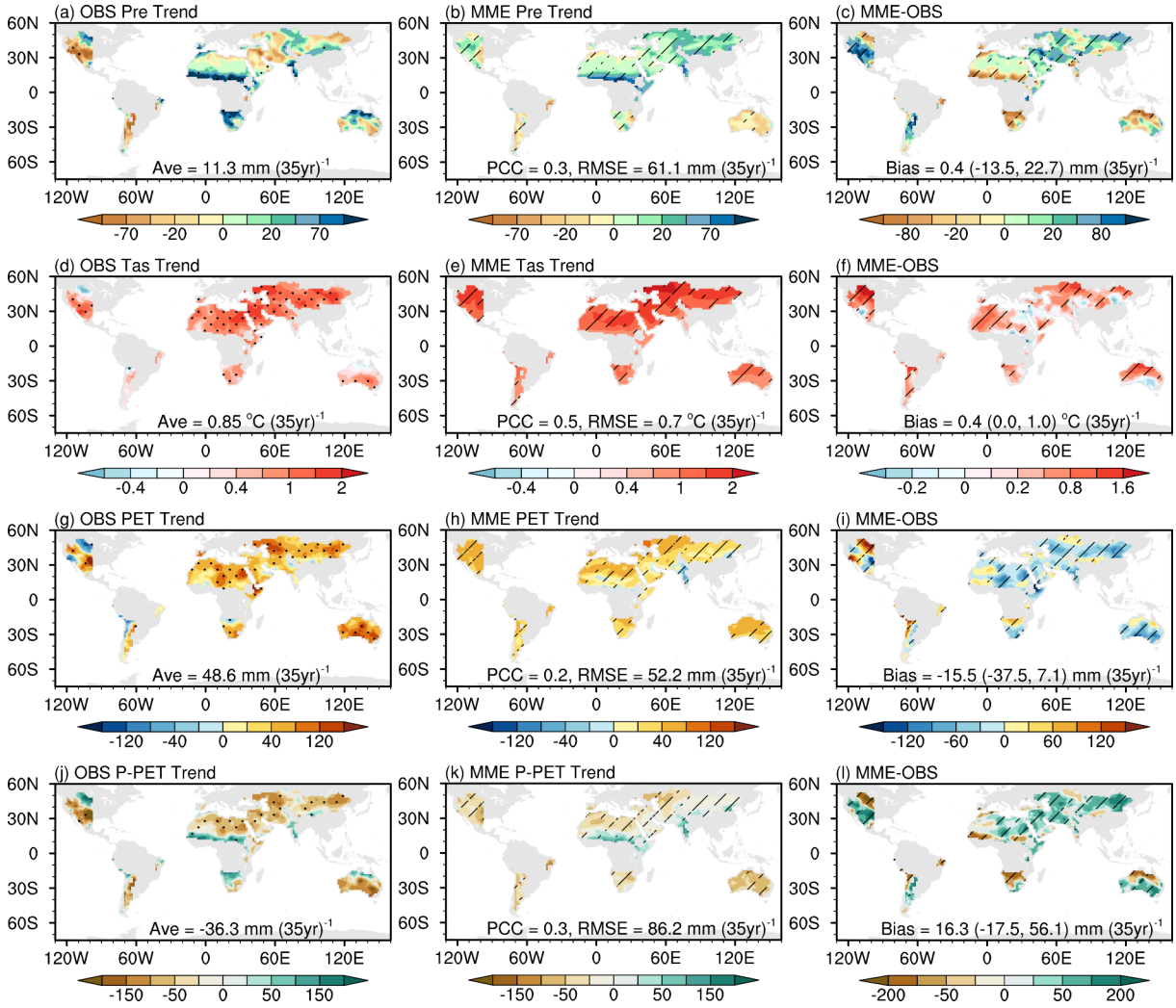

Fig. 3. Same as in Fig. 1, but for the long-term trend in four meteorological elements during 1980–2014. (a–c) Annual precipitation [units: mm (35 yr)$^{-1}$], (d–f) annual mean temperature [units: °C (35 yr)$^{-1}$], (g–i) annual potential evapotranspiration [PET, units: mm (35 yr)$^{-1}$], (j–l) annual water balance [*P*–PET, units: mm (35 yr)$^{-1}$]. Dots in the left column denote those regions passing the 0.05 significance level, and slant hatchings in the rightmost two columns indicate that 21/27 models are of the same sign.

(Figs. 3b, c). In contrast, the increasing trend is greatly underestimated by about 80 mm (35 yr)$^{-1}$ over those observed drylands which are wetting. The simulated annual mean temperature shows an overestimated warming trend in most drylands, on average by 0.42°C (35 yr)$^{-1}$ (49% of the observation) (Figs. 3e, f), while an underestimated rising trend in PET, on average by 15.5 mm (35 yr)$^{-1}$ (32% of the observation) (Fig. 3h, i). As a result, CMIP6 models systematically overestimate the trend in annual *P*–PET by 16.3 mm (35 yr)$^{-1}$ (45% of the observation) across global drylands (Figs. 3k, l), showing a similar spatial pattern to that of annual precipitation.

As the CMIP6 models still show spread in both the mean state and variability simulations, we further assess the performances of individual models using a portrait diagram (Fig. 4). Among the three metrics, the simulated climatology generally obtains the highest scores (0.6–0.98), followed by the interannual variability (0.4–0.8); the lowest scores were obtained for the long-term trend (0.4–0.6). In terms of the four meteorological elements, the simulation skill in temperature is the highest, followed by precipitation and *P*–PET; the lowest skill was for PET. For the temperature climatology, in particular, all CMIP6 models score above 0.95, close to the perfect score of 1.0. Most models perform poorly in simulating the interannual variability of PET and the long-term trend in the four meteorological elements, with scores generally less than 0.6. Notably, the performance of MME is substantially higher than any individual model except for simulating the long-term trend for precipitation and PET.

According to the calculation method of SPEI (Vicente-Serrano et al., 2010), the probability density function (PDF) of *P*–PET can substantially affect the drought index. Thus, we investigate the performance of CMIP6 models in their ability to accurately capture the PDFs related to the water balance across global drylands. Figure 5 shows the PDFs of the 6-

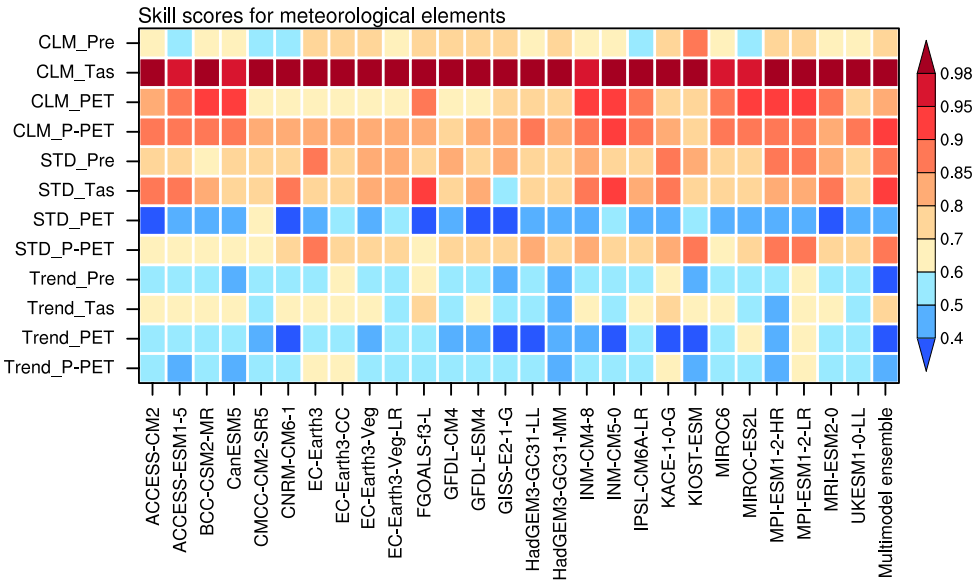

Fig. 4. Portrait diagrams of skill scores for each CMIP6 model in simulating the meteorological elements across global drylands during 1980–2014. The horizontal axis denotes 27 CMIP6 models and the multi-model ensemble mean (MME), and the vertical axis indicates the assessed metrics, including the climatology (CLM), interannual variability (STD), and long-term trend (Trend) for precipitation (Pre), temperature (Tas), potential evapotranspiration (PET) and water balance (*P*–PET). Warmer colors represent higher skills, with a perfect score of 1.0.

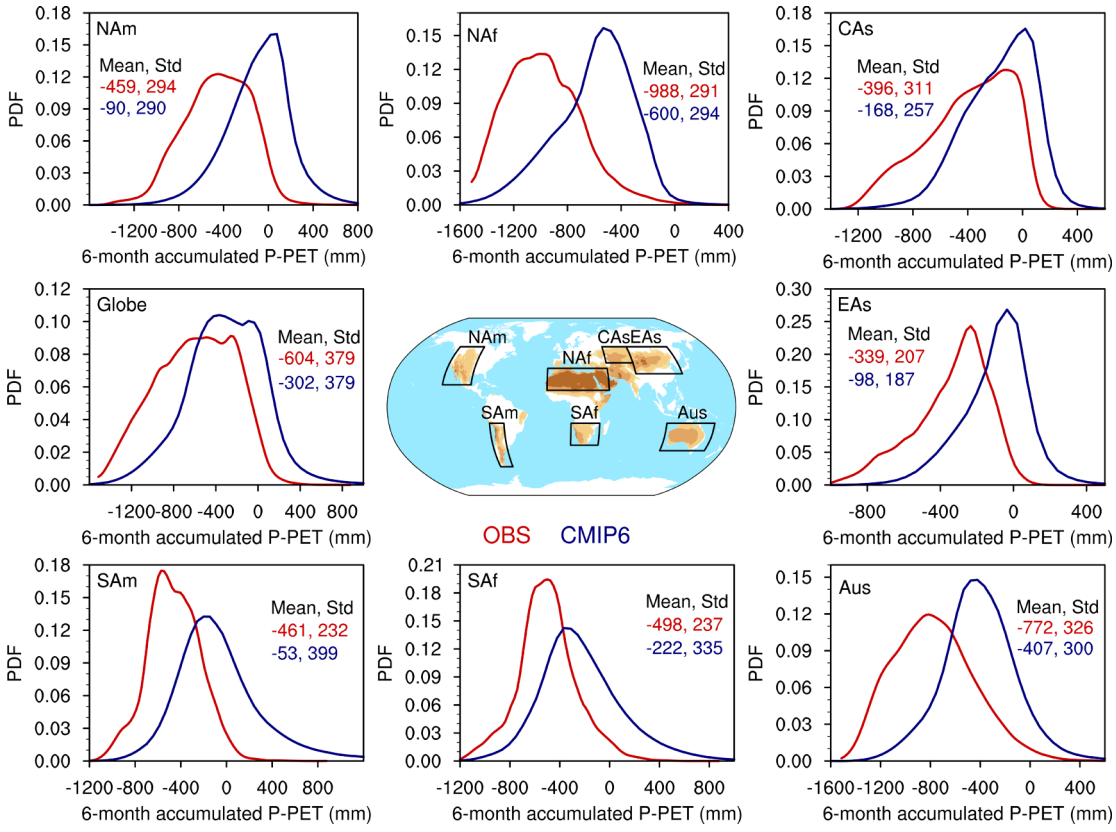

Fig. 5. Probability density functions (PDFs) of 6-month accumulated precipitation minus potential evapotranspiration (*P*–PET) for global and sub-drylands during 1980–2014. Red and blue lines denote PDFs derived from observation and CMIP6 multi-model simulations, and the numbers to the right are the mean and the standard deviation for PDFs. Boxes in the map depict the regions of seven sub-drylands, including the northern American (NAm), northern African (NAf), central Asian (CAs), East Asian (EAs), southern American (SAm), southern African (SAf), and Australian (Aus) drylands.

month accumulated *P*–PET for global and seven sub-drylands during 1980–2014. For global drylands, the simulated PDF (blue lines in Fig. 5) of *P*–PET presents an obvious rightward shift compared to the observation (red lines in Fig. 5). This suggests that much weaker water deficit conditions are simulated by CMIP6 models. The PDFs for the seven sub-drylands also show similar discrepancies with different means and standard deviations; even though the same SPEI thresholds were applied for measuring droughts, the associated water deficit conditions in CMIP6 models are quite different from the observations, which may further result in different responses of ecosystems to climate change.

3.2. *Simulation on climatological characteristics of drought events in drylands*

In this section, we examine the performance of CMIP6 models in depicting the climatological characteristics of drought events and the associated hydrothermal conditions across global drylands. The spatial patterns of the four drought categories are generally similar (figures not shown); thus, only severe droughts are shown herein to illustrate the model performances.

Figure 6 presents the climate mean spatial distributions for the severe drought intensity, occurrence, and duration in observations and the CMIP6 MME as well as their differences. In observations, the severe drought intensity in drylands is around –1.8 on average, with an evenly-distributed pattern (Fig. 6a). The observed occurrence (Fig. 6d) and duration (Fig. 6g) of severe drought are highly consistent, with an area average of 3.2 month yr^{-1} and 4.3 months, respectively, across global drylands. The most frequent and the longest-lasting severe droughts occur in the hyperarid areas of North Africa-Middle East and East Asia, with the occurrence and duration exceeding 4.0 month yr^{-1} and 5.5 months, respectively. The mean characteristics of droughts across drylands are not well captured by CMIP6 models, with the PCC of simulated drought intensity, occurrence, and duration only reaching 0.1, 0.3, and 0.1, respectively (Figs. 6b, e, h). The severe drought intensity is overestimated by –0.06 (–0.11 to –0.03) on average (Fig. 6c), while both the occurrence (Fig. 6f) and duration (Fig. 6i) are generally underestimated by CMIP6 models, with the largest biases exceeding –2 month yr^{-1} and –3 months, respectively, centered in those drylands where the most frequent and the longest lasting droughts are observed (Figs. 6d, g).

The spatial patterns for the climatology of meteorological anomalies during severe droughts from observation and CMIP6 MME and model biases are further depicted in Fig. 7. The observation shows less precipitation, warmer temperatures, higher evaporative demand and increased water deficit during severe droughts, with an area average of –11.1 mm month^{-1}, 0.6°C, 6.0 mm month^{-1}, and –17.1 mm month^{-1}, respectively, across global drylands (Figs. 7a, d, g, j). The anomalies of precipitation and *P*–PET during severe

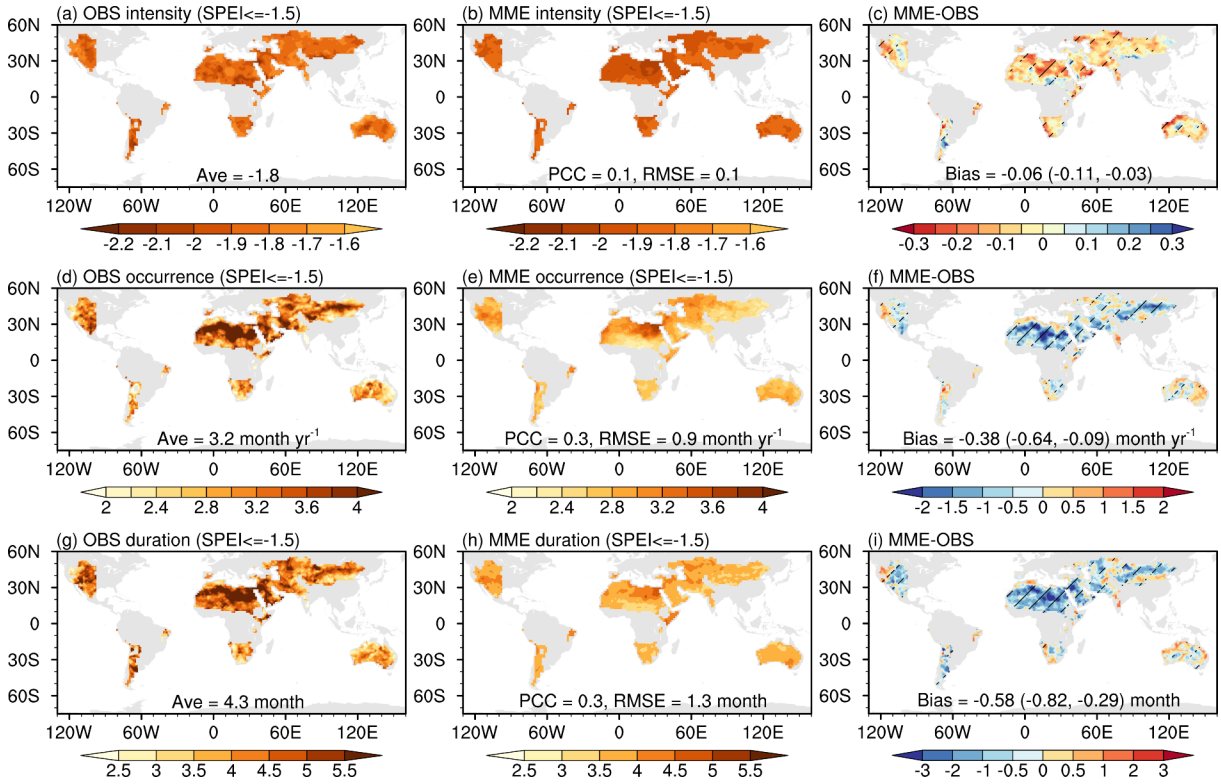

Fig. 6. Spatial patterns of the observed and simulated climatology in severe drought characteristics across global drylands during 1980–2014; (a–c) intensity, (d–f) occurrence (units: month yr^{-1}), (g–i) duration (units: month). Slant hatchings in the right column denote that 21/27 models have the same sign. Area-averaged biases are presented as MME and inter-model range between minimum and maximum, respectively.

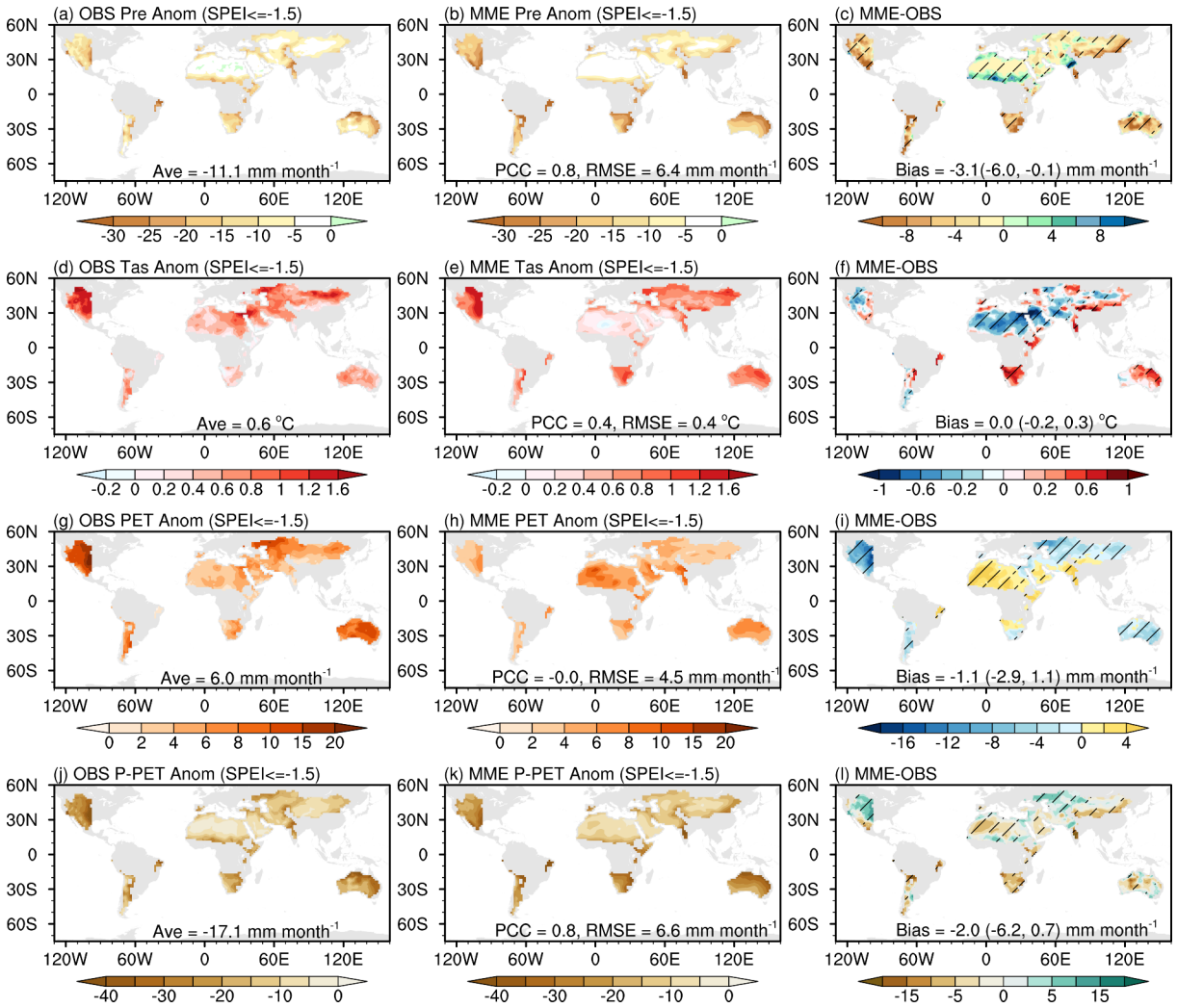

Fig. 7. Same as in Fig. 6, but for the mean meteorological anomalies composited from all severe droughts across global drylands during 1980–2014. The anomaly of each element is calculated as the previous 6-month averaged anomaly when severe drought occurs, relative to their climatology during 1980–2014 (the same below). (a–c) Precipitation (unit: mm month^{-1}), (d–f) temperature (units: °C), (g–i) potential evapotranspiration (PET, units: mm month^{-1}), and (j–l) water balance (P–PET, unit: mm month^{-1}).

droughts show a similar unevenly-distributed pattern, ranging from less than –5 and –10 mm month^{-1} over the hyperarid hinterland, to greater than –30 and –40 mm month^{-1} over semi-humid regions, respectively (Figs. 7a, j). The temperature and PET anomalies in the Northern Hemispheric drylands are generally higher than those in the Southern Hemisphere, with centers exceeding 1.6°C and 15 mm month^{-1} in the North American, central, and East Asian drylands, respectively (Figs. 7d, g).

CMIP6 models well reproduce the overall meteorological anomalies of severe droughts. The simulations agree well with observations regarding the spatial patterns of precipitation and P–PET anomalies (PCC=0.8) (Figs. 7b, k) but show large inconsistencies in terms of temperature and PET anomalies, with PCCs only reaching 0.3 and even –0.1, respectively (Figs. 7e, h). The precipitation deficit of severe drought is systematically overestimated by –3.1 mm month^{-1} (~28% of observed climatology) in most drylands except the Sahel, Mediterranean and India Peninsula regions (Fig. 7c). The biases in the temperature anomalies of severe drought show great regional differences, with positive biases (>1.0°C) present in most drylands, while negative biases (<–1.0 °C) are centered in the North Africa-Middle East drylands (Fig. 7f). The simulated PET anomaly of severe drought shows slight biases (within ±4 mm month^{-1}) in most drylands, with the largest negative bias centers (<–10 mm month^{-1}) over the North American dryland (Fig. 7i). Due to the combination of biases in precipitation and PET anomaly during severe drought, the simulated P–PET anomaly shows an overall negative bias of –4.5 mm month^{-1} (~24% of the observed climatology) in most drylands (Fig. 7i). This indicates that the magnitude in water deficit of droughts in drylands as simulated by CMIP6 models is more severe than observations.

A comparison of individual CMIP6 models in reproducing the severe drought characteristics and the corresponding

meteorological anomalies is given in Fig. 8. CMIP6 models perform poorly for the climate mean drought characteristics, with most skill scores between 0.4–0.5. Of the four meteorological anomalies during severe droughts, precipitation and *P*–PET obtain relatively higher scores of 0.6–0.8, followed by temperature with 0.4–0.6; the lowest skill scores belong to PET, for which the scores are less than 0.5. In addition, the skill scores for the other three drought categories are generally consistent with severe droughts (figures not shown).

3.3. *Simulation of the responses of dryland droughts to global warming*

To investigate the ability of CMIP6 models to reproduce the responses of droughts to global warming, the time series for area fraction and occurrence for the four drought categories across global drylands during 1980–2014 are illustrated in Figs. 9a–h. The observations show that the fractional area and occurrence for all drought categories have continuously increased since the 1980s, especially and abruptly after the late 1990s (red lines in Fig. 9a–h). CMIP6 MME (blue lines in Fig. 9a–h) can well simulate the long-term increasing trends for the drought fraction area and occurrence, but with an obvious underestimation after the late 1990s. In addition, the observed time series falls within the inter-model spreads (grey shadings in Figs. 9a–h). Hence the long-term change of dryland droughts is an externally forced signal.

We further quantitatively compare the observed and simulated long-term tendencies for the drought-affected area and occurrence, as depicted in Figs. 9i, j. The observed fraction area (occurrence) for mild, moderate, severe, and extreme droughts in drylands have increased by ~30 (~2.2), ~20 (~2.1), ~5 (~1.5), and ~1 (0.2) % (month yr^{-1}) from 1980 to 2014, respectively (red asterisks in Figs. 9i, j). CMIP6 models well reproduce their increasing tendencies (box-whisker plots in Figs. 9i, j). Consistent with the results in Figs. 9a–h, the simulated tendencies of CMIP6 MME for mild and moderate droughts are weaker than observations, with a rate of 10 % (35 yr)$^{-1}$–12 % (35 yr)$^{-1}$ and ~1 month yr^{-1} (35 yr)$^{-1}$ for fraction area and occurrence, respectively. The simulated tendencies in terms of fraction area of severe and extreme droughts agree well with observations. As seen from the spread of all models, the observed trend for severe drought occurrence is higher than inter-model spreads, while it is lower for extreme droughts.

The time series of four meteorological anomalies during four drought categories across global drylands for 1980–2014 are then presented in Fig. 10. In the observations, the three primary meteorological anomalies show an increasing trend, indicating a substantial alleviation of precipitation deficit while warmer temperatures and higher atmospheric evaporative demand intensify during all drought categories (red lines in Figs. 10a–l). This indicates that the increasing PET induced by global warming plays a dominant role in aggravating droughts in drylands. As the increased precipitation anomaly is partly offset by the elevated atmospheric evaporative demand, the water deficit conditions (*P*–PET) during droughts tend to increase only slightly (red lines in Figs. 10m–p).

CMIP6 MME (blue lines in Fig. 10) basically capture the long-term trends in the four drought-related meteorological anomalies, with their inter-model ranges (grey shadings in Fig. 10) generally covering the observations (red lines in Fig. 10). Specifically, the simulated temperature (Figs. 10e–h) and PET (Figs. 10i–l) anomalies are relatively comparable with the observations, but the magnitudes of precipitation (Figs. 10a–d) and *P*–PET (Figs. 10m–p) anomalies are overestimated, especially after the late 1990s. Additionally, the inter-model spreads of precipitation and *P*–PET anomaly are larger than the other two elements.

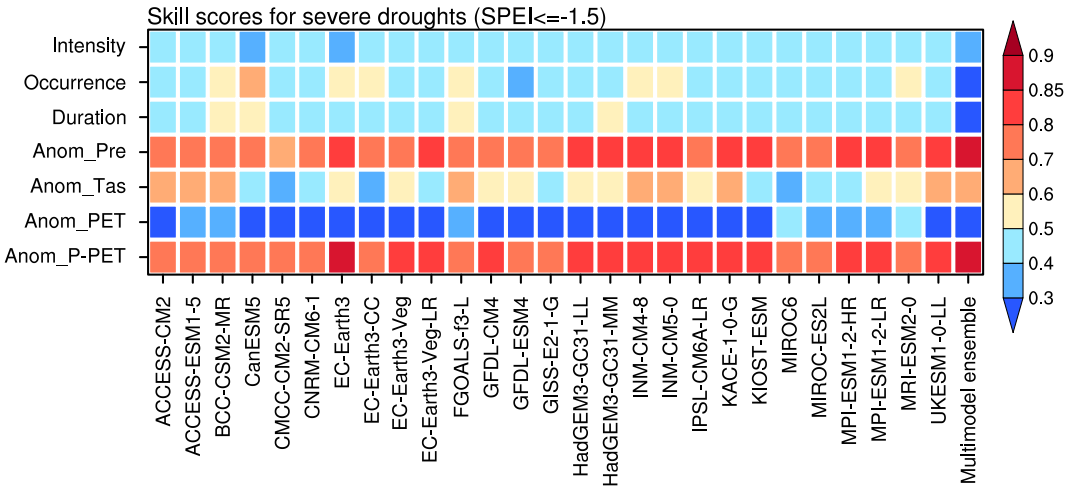

Fig. 8. Same as in Fig. 4, but for three drought metrics and four corresponding meteorological anomalies during severe droughts (SPEI≤–1.5) across global drylands during 1980–2014. The vertical axis denotes the assessed variables, including severe drought intensity, occurrence, and duration, and corresponding anomalies of precipitation (Pre), temperature (Tas), potential evapotranspiration (PET), and water balance (*P*–PET) during severe droughts.

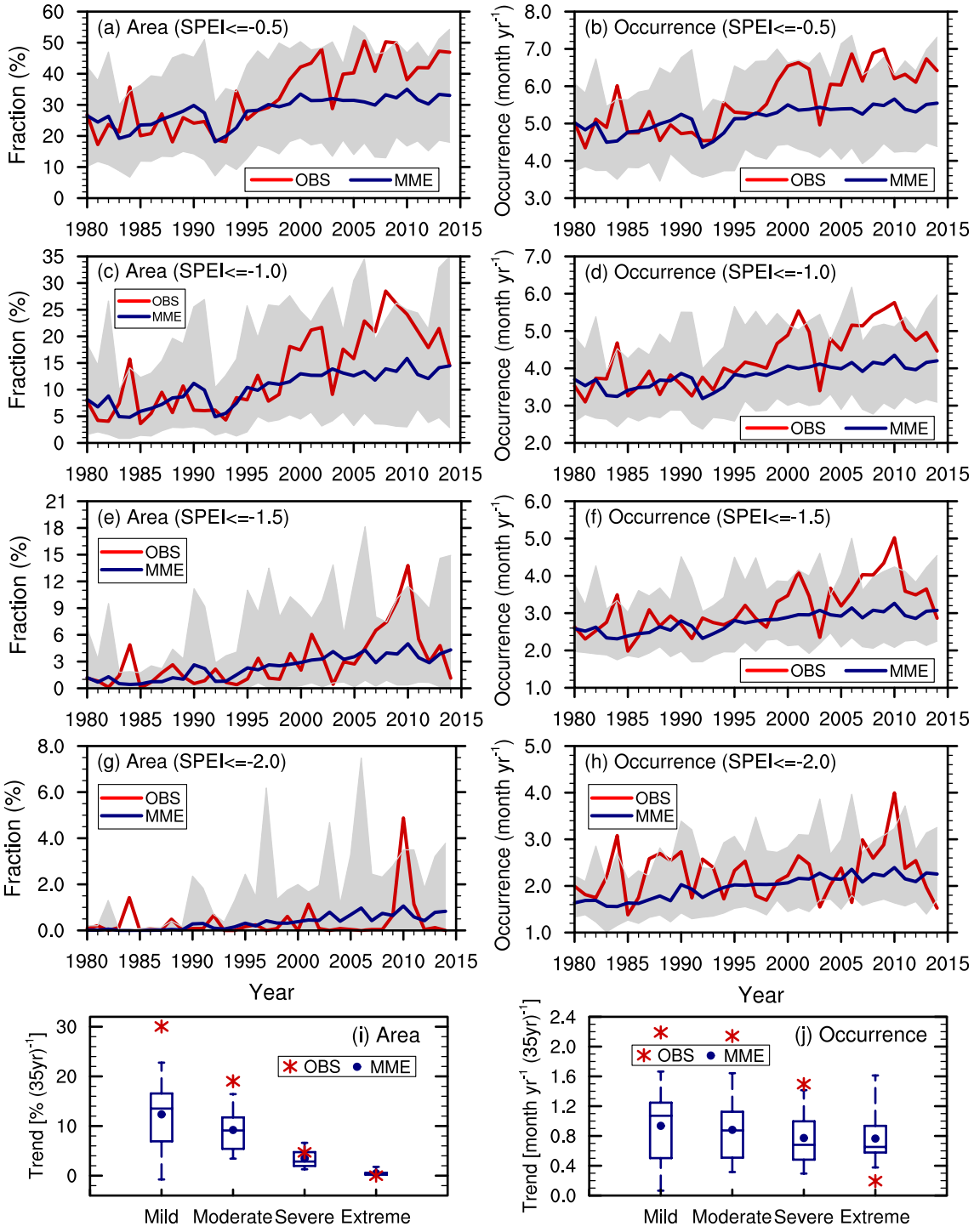

Fig. 9. Changes in metrics for different drought categories across global drylands during 1980–2014. The two columns illustrate the time series (a–h) and long-term trend (i–j) for the drought area (a, c, e, g, i, units: %) and occurrence (b, d, f, h, j, units: month yr^{-1}), respectively. (a–h) Red and blue lines denote the observations and CMIP6 multi-model ensemble mean (MME), respectively, and grey shadings denote inter-model spreads between minimum and maximum. (i–j) Box-whisker plots illustrate the minimum, first quartile, median, third quartile, and maximum of multi-model long-term tendencies. The asterisks and dots denote the observations and CMIP6 MME, respectively.

We further compare the observed and simulated long-term tendencies in the four meteorological anomalies during the four drought categories over global drylands and seven sub-drylands in Fig. 11. The observed tendencies of temperature anomalies are on the low side of the multi-model spread, whereas that of the other three meteorological anomalies are on the high side, in line with the results in Fig. 10. Among the seven sub-drylands, the observed tendencies for

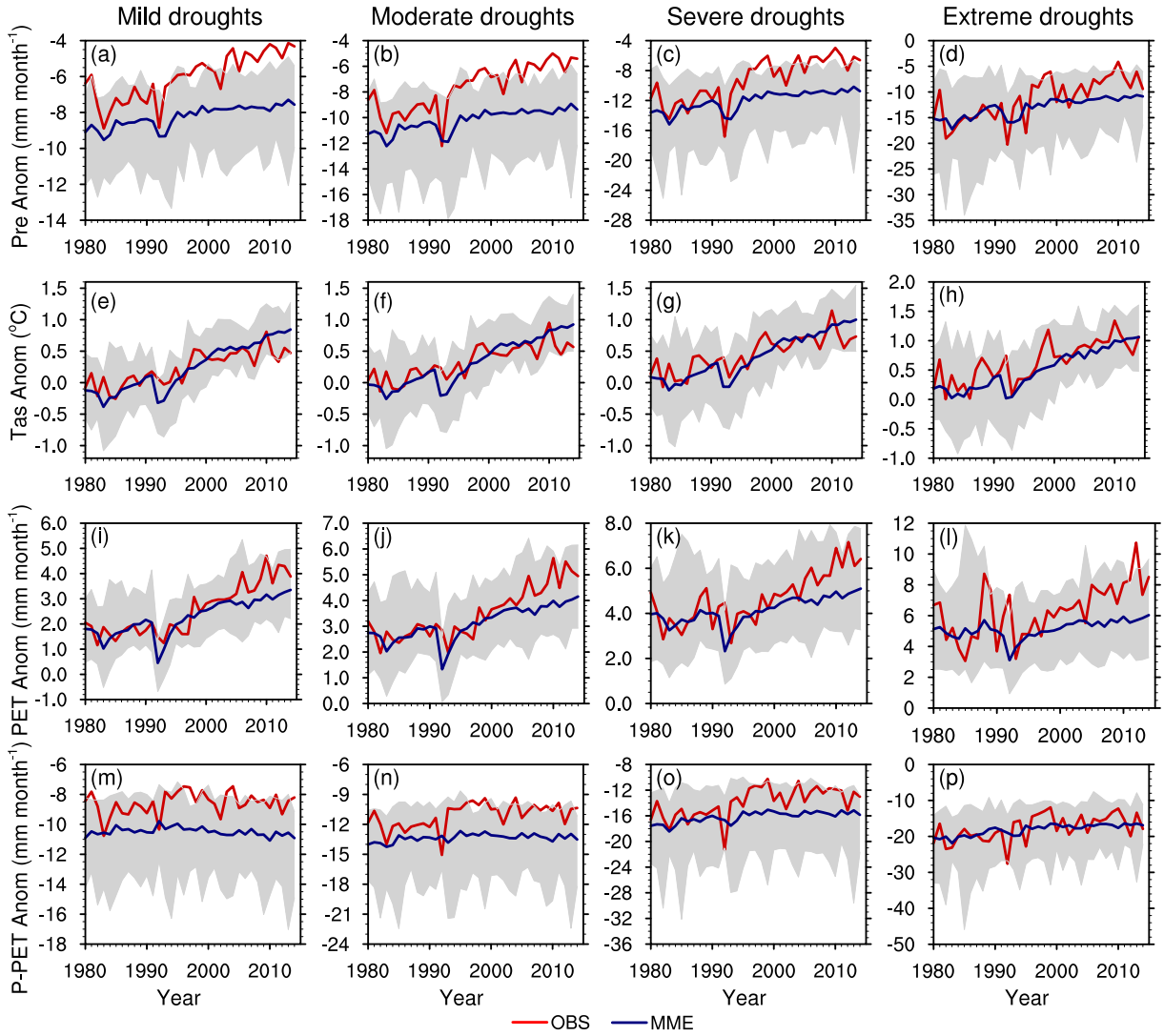

Fig. 10. Time series of meteorological anomalies during four drought categories area-averaged across global drylands over 1980–2014. The four columns are meteorological anomalies for mild (SPEI≤–0.5), moderate (SPEI≤–1.0), severe (SPEI≤ –1.5), and extreme (SPEI≤–2.0) droughts, respectively. The four rows depict the anomalies of precipitation (units: mm month^{-1}), temperature (units: °C), potential evapotranspiration (PET, units: mm month^{-1}), and water balance (*P*–PET, units: mm month^{-1}), respectively, relative to the 1980–2014 monthly climatology. Red and blue lines denote the observation and CMIP6 multi-model mean ensemble (MME), respectively, and grey shadings denote the inter-model ranges between minimum and maximum.

the four meteorological anomalies mostly fall within the inter-model ranges, except for the precipitation and PET anomaly in the North African drylands. The inter-model spreads generally tend to enlarge with increased severity of drought. For the precipitation anomaly tendencies (Fig. 11a), the inter-model spreads over the three drylands in the Southern Hemisphere (southern American, southern African, and Australian drylands) are wider than that in the Northern Hemisphere (Central Asian, East Asian, and northern American drylands), while the temperature anomalies show contrasting features (Fig. 11b). For the long-term tendencies of *P*–PET anomalies during droughts (Fig. 11d), due to the offsetting nature of the increased precipitation and PET anomalies (Fig. 11a, c), the tendencies of *P*–PET anomaly of MME in most sub-drylands (except for North American and Australian drylands) are close to 0 for mild and moderate droughts, but increase for severe and extreme droughts. Most models underestimate the increasing (decreasing) trends of *P*–PET during droughts over global (Glb) and specifically North African (NAf) drylands [during severe and extreme droughts over East Asian (EAs) and North American (NAm) drylands].

4. Summary and discussion

The performances of 27 CMIP6 models in simulating droughts and corresponding hydrothermal conditions over global drylands are elaborately documented. Both the strengths and weaknesses of CMIP6 models in the simulation of dryland droughts and the associated meteorological elements and their responses to global warming are summarized

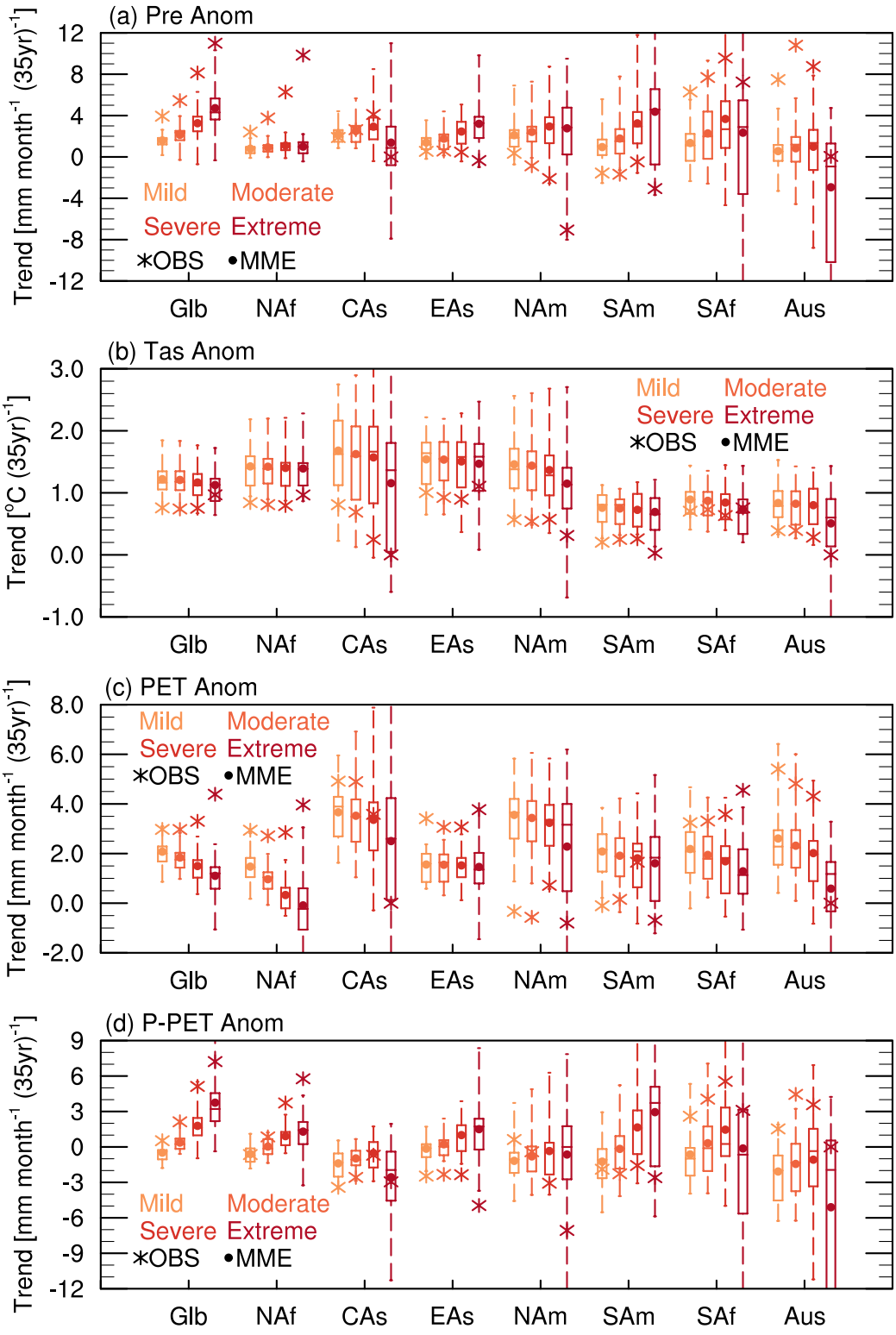

Fig. 11. Long-term tendencies for drought-related meteorological anomalies area-averaged across global drylands and seven sub-drylands during 1980–2014. (a) Precipitation [units: mm month^{-1} (35 yr)$^{-1}$], (b) temperature [units: °C (35 yr)$^{-1}$], (c) potential evapotranspiration [PET, units: mm month^{-1} (35 yr)$^{-1}$], (d) water balance [*P*–PET, units: mm month^{-1} (35 yr)$^{-1}$]. Box-whisker plots illustrate the minimum, first quartile, median, third quartile, and maximum of long-term tendencies derived from CMIP6 multi-models, with colors from shallow to deep representing mild (SPEI≤–0.5), moderate (SPEI≤–1.0), severe (SPEI≤ –1.5) and extreme (SPEI≤–2.0) droughts, respectively. The asterisks and dots denote the observations and CMIP6 multi-model ensemble mean (MME), respectively. The seven sub-drylands are the same as in Fig. 5.

as follows.

Results confirm the capability of the CMIP6 models to capture the primary characteristics of four meteorological elements, i.e., precipitation, temperature, PET, and *P*–PET, in drylands. Comparatively, the simulation skill in temperature is much higher than the other three elements. Additionally, the simulated climatology (with skill scores 0.6–0.98) for each element agrees better with observations than their interannual variations (0.4–0.8) and long-term trends (0.4–0.6). In particular, the simulated mean water balance conditions (*P*–PET) in drylands are weaker than observations by 50% (29.1%–71.7%), which results from an overestimation of annual precipitation by 33% (with a model spread of 2.3% –77.2%) and an underestimation of PET by 32% (17.5% –47.2%). Consequently, even though droughts are identified by the same SPEI thresholds, the water deficit conditions of droughts in CMIP6 models are much milder than observations.

In the context of the same SPEI thresholds, CMIP6 models are limited in capturing the observed mean drought characteristics in drylands but can reasonably reproduce the overall meteorological anomalies, including reduced precipitation, warmer temperatures, higher evaporative demand, and increased water deficit conditions. The area-averaged severe drought intensity is slightly overestimated by –0.06 (–0.11 to –0.03) over global drylands, while the occurrence and duration are underestimated by 0.38 (0.09–0.64) month yr^{-1} and 0.6 (0.3–0.8) months, respectively. In particular, the hyperarid North Africa-Middle East and East Asian regions see the most significant biases of occurrence and duration. The biases in the simulated drought characteristics may arise from more severe precipitation and water deficit during droughts in drylands, about 28% and 24% more than the observed magnitude, respectively.

The observations show that drought occurrence, fraction area, and corresponding meteorological anomalies increase continuously from 1980 to 2014. These long-term changes are well reproduced by CMIP6 MME and roughly fall within the inter-model spreads, indicating that the long-term change of dryland droughts in the past decades is an externally forced signal, but the increasing trends in drought characteristics and associated precipitation and water deficit are obviously underestimated after the late 1990s, especially for mild and moderate droughts. This suggests a weaker response of dryland droughts to global warming, as simulated by CMIP6 models. The overall increasing trends for drought-associated anomalies of precipitation, temperature, and PET further indicate that the rising evaporative demand induced by global warming is a dominant effect and is aggravating droughts in drylands.

To summarize, our results suggest that CMIP6 models are capable of reproducing the basic features of dryland droughts and corresponding hydrothermal conditions on a global scale. At the same time, the simulated water balance conditions of droughts differ greatly from observations, which may lead to a differential response among ecosystems to climate change. In addition, the model biases for meteorological elements are still large at local scales. Therefore, correcting the systematic biases inherent to GCM simulations in drought impact studies in drylands is necessary.

Acknowledgements. This work is supported by Ministry of Science and Technology of China (Grant No. 2018YFA0606501), National Natural Science Foundation of China (Grant No. 42075037) and Key Laboratory Open Research Program of Xinjiang Science and Technology Department (Grant No. 2022D04009), and the National Key Scientific and Technological Infrastructure project "Earth System Numerical Simulation Facility" (EarthLab). The CRU TS v.4.03 can be obtained from https://crudata.uea.ac.uk/cru/data/hrg/. The SPEI database v2.6 is available at https://spei.csic.es/database.html. The CMIP6 simulations can be found at https://esgf-node.llnl.gov/search/cmip6/.

REFERENCES

Allen, R. G., L. S. Pereira, D. Raes, and M. Smith, 1998: Crop evapotranspiration—Guidelines for computing crop water requirements-FAO Irrigation and drainage paper 56. https://www.fao.org/3/X0490E/x0490e00.htm

Ault, T. R., 2020: On the essentials of drought in a changing climate. *Science*, **368**, 256–260, https://doi.org/10.1126/science.aaz5492.

Cook, B. I., J. S. Mankin, K. Marvel, A. P. Williams, J. E. Smerdon, and K. J. Anchukaitis, 2020: Twenty-first century drought projections in the CMIP6 forcing scenarios. *Earth's Future*, **8**, e2019EF001461, https://doi.org/10.1029/2019EF001461.

Cherlet, M., Hutchinson, C., Reynolds, J., Hill, J., Sommer, S., von Maltitz, G. (Eds.), 2018: World Atlas of Desertification: Rethinking Land Degradation and Sustainable Land Management, Publication Office of the European Union, Luxembourg, http://dx.doi.org/10.2760/9205.

Dai, A. G., 2011: Drought under global warming: A review. *Advanced Review*, **2**, 45–65, https://doi.org/10.1002/wcc.81.

Davies, J., S. Barchiesi, C. J. Ogali, R. Welling, J. Dalton, and P. Laban, 2016: *Water in Drylands*: *Adapting to Scarcity Through Integrated Management*. IUCN.

Eyring, V., S. Bony, G. A. Meehl, C. A. Senior, B. Stevens, R. J. Stouffer, and K. E. Taylor, 2016: Overview of the coupled model intercomparison project phase 6 (CMIP6) experimental design and organization. *Geoscientific Model Development*, **9**(5), 1937–1958, https://doi.org/10.5194/gmd-9-1937-2016.

Eyring, V., and Coauthors, 2019: Taking climate model evaluation to the next level. *Nature Climate Change*, **9**, 102–110, https://doi.org/10.1038/s41558-018-0355-y.

Feng, S., and Q. Fu, 2013: Expansion of global drylands under a warming climate. *Atmospheric Chemistry and Physics Discussions*, **13**, 14 637–14 665, https://doi.org/10.5194/acpd-13-14637-2013.

Gill, J. C., and B. D. Malamud, 2014: Reviewing and visualizing the interactions of natural hazards. *Rev. Geophys.*, **52**, 680–722, https://doi.org/10.1002/2013RG000445.

Harris, I., T. J. Osborn, P. Jones, and D. Lister, 2020: Version 4 of the CRU TS monthly high-resolution gridded multivariate climate dataset. *Scientific Data*, **7**, 109, https://doi.org/10.1038/s41597-020-0453-3.

Huang, J. P., H. P. Yu, X. D. Guan, G. Y. Wang, and R. X. Guo, 2016: Accelerated dryland expansion under climate change. *Nature Climate Change*, **26**, 166–171, https://doi.org/10.1038/NCLIMATE2837.

Hulme, M., 1996: Recent climatic change in the world's drylands. *Geophys. Res. Lett.*, **23**, 61–64, https://doi.org/10.1029/95GL03586.

Kendall, M. G., 1955: *Rank Correlation Methods*. 2nd ed. C. Griffin, 86–91.

Liu, X. L., C. X. Li, T. B. Zhao, and L. Han, 2020: Future changes of global potential evapotranspiration simulated from CMIP5 to CMIP6 models. *Atmospheric and Oceanic Science Letters*, **13**, 568–575, https://doi.org/10.1080/16742834.2020.1824983.

Mann, H. B., 1945: Non-parametric tests against trend. *Econometrica*, **13**, 245–259, https://doi.org/10.2307/1907187.

Middleton, N., and D. Thomas, 1992: *World Atlas of Desertification*. UNEP.

Monteith, J. L., 1965: Evaporation and Environment. *Symposia of the Society for Experimental Biology*, **19**, 205–234.

Penman, H. L., 1948: Natural evaporation from open water, bare soil and grass. *Proceedings of the Royal Society A: Mathematical, Physical and Engineering Sciences*, **193**, 120–145, https://doi.org/10.1098/rspa.1948.0037.

Peters-Lidard, C. D., D. M. Mocko, L. Su, D. P. Lettenmaier, P. Gentine, and M. Barlage, 2021: Advances in land surface models and indicators for drought monitoring and prediction. *Bull. Amer. Meteor. Soc.*, **102**, E1099–E1122, https://doi.org/10.1175/BAMS-D-20-0087.1.

Piao, S. L., X. P. Zhang, A. P. Chen, Q. Liu, X. Lian, X. H. Wang, S. S. Peng, and X. C. Wu, 2019: The impacts of climate extremes on the terrestrial carbon cycle: a review. *Science China Earth Sciences*, **62**, 1551–1563, https://doi.org/10.1007/s11430-018-9363-5.

Sen, P. K., 1968: Estimates of the regression coefficient based on Kendall's Tau. *Journal of the American Statistical Association*, **63**, 1379–1389, https://doi.org/10.1080/01621459.1968.10480934.

Seo, K. H., J. Ok, J. H. Son, and D. H. Cha, 2013: Assessing future changes in the East Asian summer monsoon using CMIP5 coupled models. *J. Climate*, **26**, 7662–7675, https://doi.org/10.1175/JCLI-D-12-00694.1.

Sherwood, S., and Q. Fu, 2014: A drier future? Global warming is likely to lead to overall drying of land surfaces *Science*, **343**, 737–739, https://doi.org/10.1126/science.1247620.

Sivakumar, M. V. K., R. Lal, R. Selvaraju, and I. Hamdan, 2013: *Climate Change and Food Security in West Asia and North Africa*. Springer, https://doi.org/10.1007/978-94-007-6751-5.

Theil, H., 1992: A rank-invariant method of linear and polynomial regression analysis. *Henri Theil's Contributions to Economics and Econometrics*, B. Raj and J. Koerts, Eds., Springer, 345–381, https://doi.org/10.1007/978-94-011-2546-8.

Ukkola, A. M., A. J. Pitman, M. G. De Kauwe, G. Abramowitz, N. Herger, J. P. Evans, and M. Decker, 2018: Evaluating CMIP5 model agreement for multiple drought metrics. *Journal of Hydrometeorology*, **19**, 969–988, https://doi.org/10.1175/JHM-D-17-0099.1.

Ukkola, A. M., M. G. De Kauwe, M. L. Roderick, G. Abramowitz, and A. J. Pitman, 2020: Robust future changes in meteorological drought in CMIP6 projections despite uncertainty in precipitation. *Geophys. Res. Lett.*, **47**, e2020GL087820, https://doi.org/10.1029/2020GL087820.

Vicente-Serrano, S. M., S. Beguería, and J. I. López-Moreno, 2010: A multiscalar drought index sensitive to global warming: The standardized precipitation evapotranspiration index. *J. Climate*, **23**, 1696–1718, https://doi.org/10.1175/2009JCLI2909.1.

Vicente-Serrano, S. M., and Coauthors, 2013: Response of vegetation to drought time-scales across global land biomes. *Proceedings of the National Academy of Sciences of the United States of America*, **110**, 52–57, https://doi.org/10.1073/pnas.1207068110.

Vicente-Serrano, S. M., S. M. Quiring, M. Peña-Gallardo, S. S. Yuan, and F. Domínguez-Castro, 2020: A review of environmental droughts: Increased risk under global warming. *Earth-Science Reviews*, **201**, 102953, https://doi.org/10.1016/j.earscirev.2019.102953.

White, R. P., and J. Nackoney, 2003: *Drylands*, *People*, *and Ecosystem Goods and Services*: *A Web-Based Geospatial Analysis*. World Resources Institute.

WMO, 2021: *WMO Atlas of Mortality and Economic Losses from Weather*, *Climate and Water Extremes* (*1970–2019*). WMO.

Zhao, T. B., and A. G. Dai, 2017: Uncertainties in historical changes and future projections of drought. Part II: Model-simulated historical and future drought changes. *Climatic Change*, **144**, 535–548, https://doi.org/10.1007/s10584-016-1742-x.

Zhao, T. B., and A. G. Dai, 2022: CMIP6 model-projected hydroclimatic and drought changes and their causes in the twenty-first century. *J. Climate*, **35**, 897–921, https://doi.org/10.1175/JCLI-D-21-0442.1.

Zhao, T. B., L. Chen, and Z. G. Ma, 2014: Simulation of historical and projected climate change in arid and semiarid areas by CMIP5 models. *Chinese Science Bulletin*, **59**, 412–429, https://doi.org/10.1007/s11434-013-0003-x.